Journal of Materials Research and Technology 33 (2024) 3439–3451

Contents lists available at ScienceDirect

Journal of Materials Research and Technology

journal homepage: www.elsevier.com/locate/jmrt

Elastocaloric effect of NiTi shape memory alloys manufactured by laser powder bed fusion

Changyong Chen [a,b], Ze Pu [a,b], Bailiang Qin [a,b], Pengbo Wang [a,b], Congrui Yang [a,b], Kangcheung Chan [a,b,*]

[a] State Key Laboratory of Ultra-precision Machining Technology, Department of Industrial and Systems Engineering, The Hong Kong Polytechnic University, Hong Kong, China

[b] Research Institute for Advanced Manufacturing, Department of Industrial and Systems Engineering, The Hong Kong Polytechnic University, Hong Kong, China

ARTICLE INFO

Keywords:
Additive manufacturing
Laser powder bed fusion
NiTi alloys
Superelasticity
Elastocaloric effects

ABSTRACT

To address the challenges posed by the complex processing of NiTi alloys, the additive manufacturing technology has been employed for the preparation of NiTi alloys samples. Up to now, there is limited research on the elastocaloric effects of NiTi alloys manufactured by LPBF. This study focused on the utilization of laser powder bed fusion (LPBF) to fabricate NiTi samples, with a particular emphasis on the influence of laser power, scanning speed and hatch spacing on the microstructure and properties of NiTi alloys. The results indicated that the process parameters affect the stress hysteresis of superelasticity by influencing the Ni content in the NiTi alloys. The higher Ni content, the lower the stress hysteresis. In addition, the critical stress for plastic deformation of the texture in the <001> direction in NiTi alloys is the smallest. When only the *P* was changed, the proportion of the texture in the <001> direction in the sample increased with the increase of *P*, the proportion of plastic deformation increased, and the degree of recovery also gradually decreased. Furthermore, at a specific temperature, 10 K higher than the end temperature of austenite transformation, each sample exhibited good superelasticity. In particular, the 1st cooling capacity of the sample with the best elastocaloric effect reached 11.0 K, which was superior to other results obtained by LPBF under similar compressive strain levels.

1. Introduction

Near equiatomic NiTi alloys possess excellent shape memory effect and superelasticity making it widely used in fields such as medicine and aerospace 1,2. However, due to the challenges in machining, NiTi alloys are typically limited to simple shapes such as pipes, wires, and bars, making it difficult to fabricate complex structural components [3–6]. Additive manufacturing technology offers great flexibility, allowing for the preparation of samples with complex structures, presenting a promising solution for materials like NiTi alloys that are difficult to shape [7,8].

Unlike traditional methods of preparing NiTi alloys, LPBF introduces micro defects (e.g., spheroidization, keyholes, and incomplete fusion) and macro defects (e.g., delamination, cracks, and warping) caused by the laser's action. Additionally, the energy density of commonly used lasers is distributed in a Gaussian pattern, resulting in uneven temperature distribution during the formation of the molten pool. This uneven distribution affects the element evaporation and element distribution in the alloy matrix, thereby significantly impacting the phase transformation behavior of LPBF NiTi alloys [9]. Hence, optimizing process parameters is crucial in LPBF preparation of NiTi alloys to prevent these processing defects and ensure the production of high-quality NiTi alloys parts that meet the functional requirements.

Guan [10] conducted an initial investigation into the possibility of using Ni and Ti elemental powders as raw materials for producing NiTi alloys through the LPBF method. The study examined the influence of laser power and scanning speed on the formability of NiTi alloys and found that samples with a linear energy density ranging from 0.38 to 1.44 J/mm exhibited better formability. However, the best-formed NiTi alloys sample in Guan's experiment contained numerous pores and micro-cracks, indicating the need for further optimization of process parameters. Additionally, the microstructure analysis of NiTi alloys samples, including parameters such as grain size, texture, and precipitation, was not carried out in Guan's study. Furthermore, Guan did not

* Corresponding author. State Key Laboratory of Ultra-precision Machining Technology, Department of Industrial and Systems Engineering, The Hong Kong Polytechnic University, Hong Kong, China.

E-mail address: kc.chan@polyu.edu.hk (K. Chan).

https://doi.org/10.1016/j.jmrt.2024.09.081
Received 5 April 2024; Received in revised form 11 September 2024; Accepted 12 September 2024
Available online 28 September 2024

study the superelasticity and elastocaloric effect of NiTi alloys prepared by LPBF. These contents need to be further studied.

In a separate study, Xue et al. [11] investigated the forming process window of NiTi alloys and correlated process parameters with forming quality using the Eagar Tsai model. The results revealed four distinct regions in the relationship between "laser power and scanning speed" and "forming quality," namely the spheroidization zone, keyhole formation zone, incomplete melting zone, and good forming quality zone. The findings indicated that the regions of good forming quality for NiTi powders with different compositions consistently included high power combined with high scanning speed areas and low power combined with low scanning speed areas, which aligns with the earlier statistical findings mentioned above. However, elastocaloric effect of NiTi alloys prepared by LPBF did not be study in their experiment.

Additionally, the parameters used in the LPBF process have a significant impact on the size and morphology of grains. Saedi et al. [12] conducted a study on the microstructure changes of LPBF NiTi alloys under various scanning and power conditions, and observed that the process parameters directly influence the size and morphology of grains. Different combinations of laser power and scanning speed can result in distinct grain morphologies. Specifically, when moderate laser energy density levels (55.5–79.4 J/mm^3) and laser power conditions exceeding 200 W are used, many square grains are formed in the NiTi alloys matrix, whereas elongated "S" shaped grains are obtained in the NiTi alloys matrix when low laser power (energy density levels higher than 123.4 J/mm^3) of 100 W is employed. Gao et al. [13] also discovered that the hatch spacing in the LPBF process can significantly impact the size and morphology of grains.

Moreover, the process parameters not only affect the formability and microstructure of the sample but also naturally influence its phase transformation temperature, mechanical properties, and other characteristics. There are several factors that can cause changes in the phase transformation temperature of NiTi alloys prepared through LPBF, such as variations in the Ni/Ti atomic ratio in the matrix due to different process parameters [14], the presence of residual stress in the matrix [15], and the precipitation of precipitates [16,17]. Additionally, subsequent heat treatment is an effective method for controlling the phase transformation temperature of LPBF NiTi alloys [18–20]. These research findings offer the potential to obtain a wider range of LPBF NiTi alloys with controllable properties.

Furthermore, process parameters have a significant impact on the superelasticity and elastocaloric effects of NiTi alloys. Cong et al. [21] investigated the effect of LPBF process parameters on the elastocaloric effect of NiTi alloy, but only the hatch spacing parameter has been studied. In addition, the largest cooling capacity of the as-fabricated sample was about 9.4 K. This value is not very large, which means that the elastocaloric effects of NiTi alloys prepared by LPBF has the potential to be further explored.

The elastocaloric effect of NiTi alloys prepared by conventional methods has been extensively studied and widely reported. However, there are few studies on the elastocaloric effect of NiTi alloys prepared by LPBF. Only four papers have been published [21–24], and the relevant research data are not sufficient. Cong et al. [21] were the first to report the caloric effect test results of the as-built NiTi alloys prepared by LPBF, and the temperature drop during unloading was approximately 9.8 K. Kordizadeh et al. [22,23] tested the elastocaloric effect of the LPBFed NiTi alloys. The temperature drop during unloading could reach 10.5 K, but the test temperature was around 50 °C, which is not near room temperature. Ma et al. [24] also tested the elastocaloric effect of the LPBFed NiTi alloys, and the temperature drop during unloading was only 6.5 K. However, it is important to further improve the elastocaloric effect of the LPBFed NiTi alloys and to fully understand the impact of process parameters on the superelasticity and elastocaloric effects of the alloys. In addition, the relationship between the composition of NiTi alloys and their elastocaloric effect is still uncertain. It is not easy to predict the maximum temperature drop when the elastocaloric effect occurs based on the composition. Therefore, this paper aims to address the above issues.

In this study, two sets of experiments were conducted. Group I examined the influence of laser power and scanning speed on the formability of NiTi alloys and preliminarily identified optimized process windows. Basing upon the results of Group I, the impact of hatch spacing on the formability of NiTi alloys will be continue to investigated in Group II, and the optimal combination of process parameters will be explored at the same time. Concurrently, the effects of process parameters on the microstructure and mechanical properties of NiTi alloys have been studied. Moreover, based on the findings of existing studies in the literature and preliminarily established a functional relationship was established between the composition of binary NiTi alloys and the theoretical maximum temperature drop when the elastocaloric effect occurs.

2. Experimental procedure

The NiTi alloys powder used in this study was obtained from Liaoning Guanda New Material Technology Co., LTD (Anshan city, Liaoning Province, China). The chemical composition of the NiTi alloys powder is presented in Table 1. The content of Ti, Ni, Cu, Co, Cr, Nb and Fe were determined by inductively coupled plasma-atomic emission spectroscopy (ICP-AES). The element content of carbon was detected by high frequency combustion method with infrared measurement. The content of O and N were measured by infrared method after fusion under inert gas. It is worth noting that the powder exhibits low levels of impurities such as O, N, H, and C. The powder was produced using the PREP (plasma rotating electrode method) technique (Xi'an Sailon Additive Technology Co., Ltd. Xian, China, SLPA-N50), and its morphology is depicted in Fig. 1(a). The powder particles exhibit a small cellular crystal structure with excellent sphericity. Additionally, the individual particles have a clean and smooth surface, devoid of any undesirable features such as satellite or hollow balls. The average particle size, represented by D50, is 37 μm. The particle size distribution is relatively uniform, making it highly suitable for the LPBF process.

Fig. 1(b) shows the DSC phase transformation curve of the powder, illustrating a one-step phase transformation process during temperature variations. Specifically, the cooling process involves a B2→B19' phase transformation, while the heating process involves a B19'→B2 phase transformation. Furthermore, the XRD results in Fig. 1(c) confirm that the NiTi alloys powder consists solely of the B2 austenite phase.

Fig. 1(d) depicts the partition scanning strategy employed in this experiment. The primary objective of this strategy is to minimize overlap between scanning methods in each layer, thereby preventing the growth of columnar crystals along the building direction. To achieve this, a rotation angle is designated for each layer's scanning direction, which is not evenly divisible by 360°. Moreover, efforts are made to ensure a substantial interval between rotation angles of successive layers. For this experiment, a rotation angle of 67° was chosen. Additionally, the laser follows a short straight "S" path within each scanning band. The key process parameters involved include hatch spacing, layer thickness, laser power, and scanning speed.

Fig. 1(e) and (f) display the macroscopic morphology of the NiTi alloys samples manufactured using LPBF in this experiment. The samples exhibit excellent formability and exhibit no issues such as cracking, warping, or collapse. The surfaces demonstrate good brightness and flatness, indicating that the selected process parameters for the experiment are suitable.

In this experiment, two groups of samples were manufactured: group I and group II. Group I had variation parameters of laser power (P) and scanning speed (v), which are detailed in Table 2. The relative density of all samples in group I was calculated, and the six parameter groups with the highest relative density were selected as the basic parameters for group II. The objective of group II was to investigate the effect of hatch spacing on the microstructure and properties of NiTi alloys. The specific

Table 1
Chemical composition of NiTi alloys power for LPBF (mass fraction/%).

No.	Ti	Ni	C	Co	Cu	Cr	Fe	Nb	O + N	H
Requested	Balance	54.5–57.00	≤0.05	≤0.05	≤0.01	≤0.01	≤0.05	≤0.025	≤0.05	≤0.005
Tested	Balance	55.64	≤0.005	≤0.0005	≤0.0046	≤0.0005	≤0.0014	≤0.005	≤0.05	0.0017

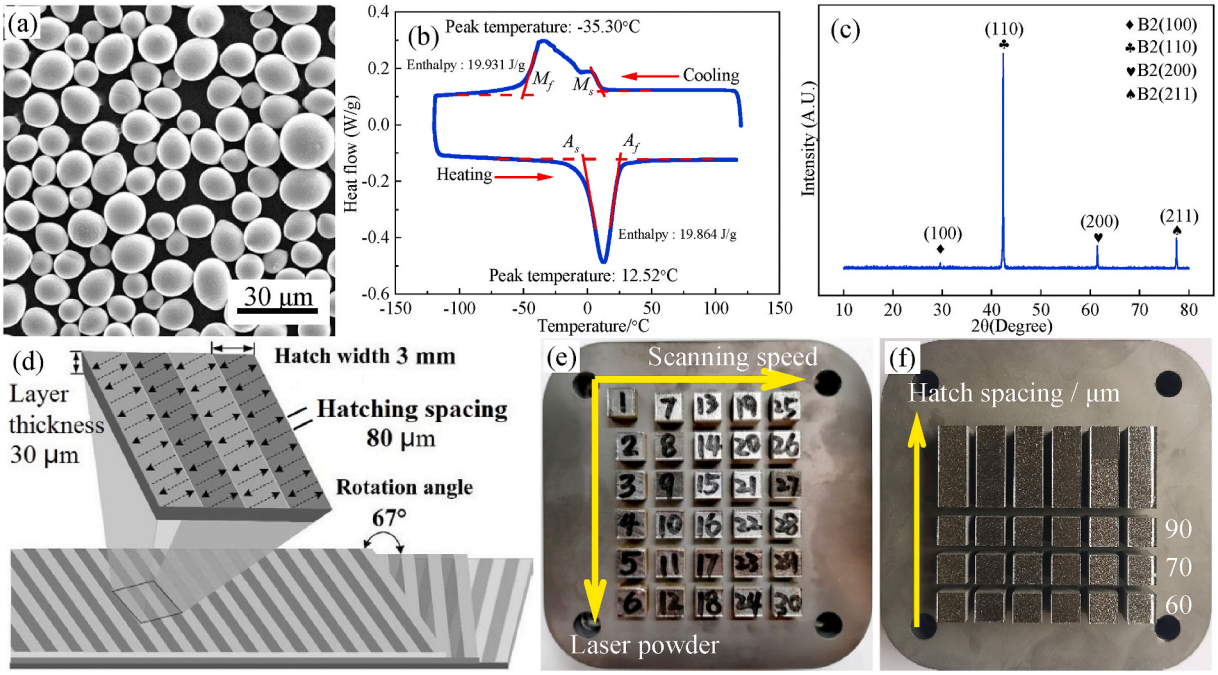

Fig. 1. (a) The microstructure of NiTi alloys powder, (b) DSC result of NiTi powder; (c) XRD result of NiTi powder; (d) Schematic diagram of laser scanning method. NiTi alloys experimental samples prepared by LPBF: (e) The variables are laser power and scanning speed.; (f) The variable is hatch spacing.

Table 2
Process parameters for LPBF preparation of NiTi alloys, group I.

No.	*P*	*v*	*ED*	No.	*P*	*v*	*ED*	No.	*P*	*v*	*ED*	No.	*P*	*v*	*ED*	No.	*P*	*v*	*ED*
I-1	100	200	208	I-7	100	400	104	I-13	100	600	69	I-19	100	800	53	I-25	100	1000	42
I-2	120		250	I-8	120		125	I-14	120		83	I-20	120		63	I-26	120		50
I-3	140		292	I-9	140		146	I-15	140		97	I-21	140		73	I-27	140		58
I-4	160		333	I-10	160		167	I-16	160		111	I-22	160		83	I-28	160		67
I-5	180		375	I-11	180		188	I-17	180		125	I-23	180		94	I-29	180		75
I-6	200		417	I-12	200		208	I-18	200		139	I-24	200		104	I-30	200		83

Note: *P*- Laser power/W; *v*- Scanning speed/mm/s; *ED*-Energy density/J/mm^3.

parameters for group II can be found in Table 3. In this experiment, the Archimedes drainage method was used to test the relative density of the samples.

The phase identification was performed at room temperature using X-ray diffraction (XRD, Rigaku Smart Lab 9 kW) with Cu Kα radiation. The phase transformation temperatures were determined by differential scanning calorimetry (DSC, NETZSCH DSC 204) with heating and cooling rates of 10 K/min. The microstructure was examined using a ZEISS optical microscope. The crystallographic orientation and elemental distribution were investigated by electron backscatter diffraction (EBSD) and energy dispersive spectroscopy (EDS) analysis, respectively, using SEM (TESCAN MIRA). The precipitates in the aged samples were studied by transmission electron microscopy (TEM, JEOL JEM-2100F) operated under an accelerating voltage of 200 kV.

Table 3
Process parameters for LPBF preparation of NiTi alloys, group II.

No.	*h*	*ED*	No.	*h*	*ED*	No.	*h*	*ED*	*P*	*v*	Basic heat-No.	*h*	*ED*
II-1	60	77	II-7	70	66	II-13	90	52	140	1000	I-27	80	58
II-2		84	II-8		72	II-14		56	120	800	I-20		63
II-3		89	II-9		77	II-15		60	160	1000	I-28		67
II-4		92	II-10		79	II-16		61	100	600	I-13		69
II-5		97	II-11		83	II-17		65	140	800	I-21		73
II-6		111	II-12		95	II-18		74	120	600	I-14		83

Note: *P*- Laser power/W; *v*- Scanning speed/mm/s; *h*-hatch spacing/μm; *ED*-Energy density/J/mm^3.

The mechanical properties and elastocaloric effect of the SLM fabricated samples were studied by compression tests using a mechanical testing machine (Zwick/Roell, 20 KN). The directly fabricated samples ($\Phi 3 \times 6$ mm^3), without any further machining, were used. The stress-strain curves were measured with a low strain rate of 10^{-4} s^{-1}. To ensure the accuracy and reliability of the data, a non-contacting laser extensometer was used to record the strain. The elastocaloric effect, ΔT, during compression process was monitored by three 5 TC-TT-K-40 K-type thermocouples sticked to sample surface. For an adiabat condition, a high strain rate of 10^{-1} s^{-1} was applied during elastocaloric test. The temperature data were recorded by the OM-DAQ-USB-2401 data acquisition module. A relatively high strain rate was used for unloading to approach the adiabatic condition.

3. Results

3.1. Porosities and cracks in the microstructure of NiTi alloys samples

When the laser energy density is too high, both many porosities and micro-cracks will be generated in the sample. These elongated micro-cracks propagate along the edges of the laser trajectory, as shown in Fig. 2(a). The formation of micro-cracks during the preparation of NiTi alloys by LPBF can be attributed to the ultra-high heating and cooling rates of the molten pool during the LPBF forming process, which can reach 10^3–10^7 K/s [21]. These rapid temperature changes lead to the accumulation of residual thermal stress during the LPBF process. Additionally, simulation research by Parry et al. [25] indicates that this residual thermal stress is generated and distributed along the construction direction during the LPBF preparation of metal parts. When the accumulated thermal stress exceeds the yield strength of LPBF NiTi alloys, micro-cracks gradually form and expand, eventually connecting with each other.

As the laser energy density gradually decreases, micro-cracks disappear first in the samples. Simultaneously, the number and size of porosities gradually decrease. It is important to note that the number and size of porosities in the sample reach their minimum level when the laser energy density is approximately 60 J/mm^3, as shown in Fig. S1. With further decreases in energy density, the sample showed many defects (Fig. 2(b)), including irregularly shaped holes (Fig. 2(c)) and un-melted powder (Fig. 2(d)).

Comparing Fig. 2(a) and (c), too high or too low laser energy density will lead to defects in the NiTi alloys sample. The former is mostly spherical holes, which is mainly caused by element evaporation, while the latter is irregular in shape, which is mainly caused by the powder not being completely melted.

3.2. Densification of NiTi alloys samples

The relative density of the two sample groups varies with the process parameters, as illustrated in Fig. 3. For group I (Fig. 3(a)), it is evident that the energy density directly affects the relative density. Specifically, when the energy density exceeds 70 J/mm^3 (No. I-13), the relative density increases as the energy density decreases. This is primarily due to the formation of porosities in the sample caused by powder evaporation at high energy densities. The number and density of these porosities increase with higher energy densities, resulting in a lower overall density of the sample. Conversely, when the energy density falls below 70 J/mm^3, the relative density decreases as the energy density decreases. This is because a small amount of powder is not completely melted at lower energy densities, leading to an increase in the amount of un-melted powder and a subsequent decrease in density. Based on the relative density analysis (Fig. 3(a)) and metallographic photos of the porosities (Figure S1 and Figure S2), the samples with the highest relative density are No. I-13, No. I-14, No. I-20, No. I-21, No. I-27, and No. I-28, which are highlighted with red dashed boxes in Fig. S1.

For group II (Fig. 3(b)), a similar pattern is observed. The optimal energy density range for achieving the highest relative density is approximately 60–70 J/mm^3.

3.3. Molten pool, grains and columnar crystal in the microstructure of NiTi alloys

The morphology of the molten pool, as shown in Fig. 4, exhibits a typical semi-elliptical shape, indicating that it was formed through

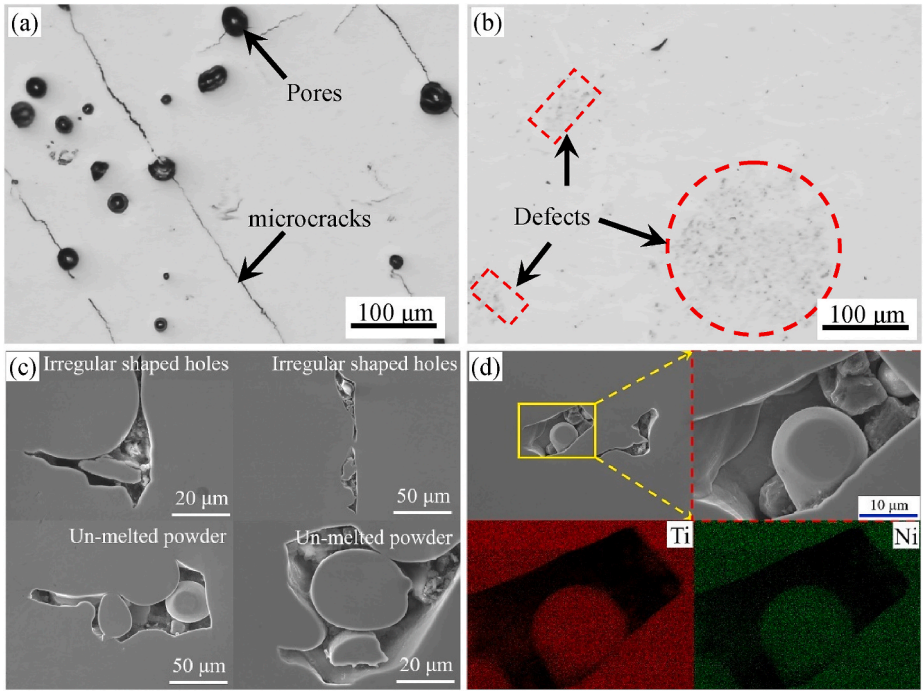

Fig. 2. The microstructure morphology of samples: (a) the crack in sample with high energy density (No. I-1); (b) The OM morphology of un-melted powder in sample with low energy density (No. I-25); (c) Defects in No. I-25 sample; (d) Mapping of un-melted powders in No. I-25 sample.

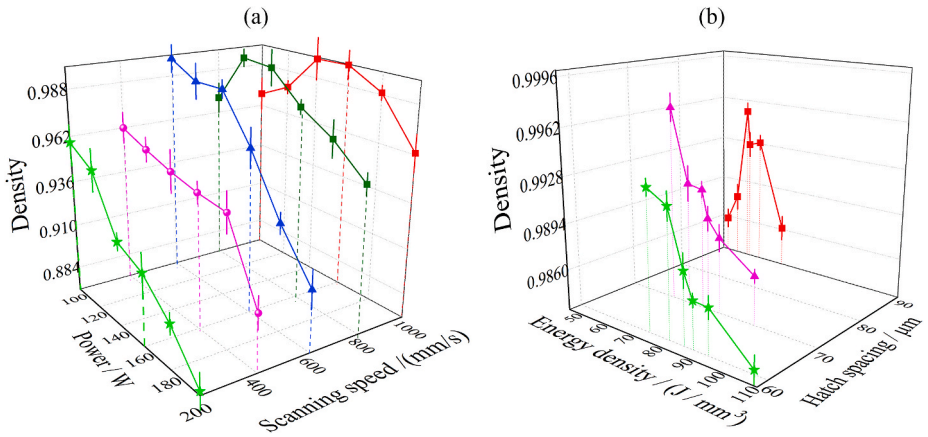

Fig. 3. Densification of NiTi alloys samples: (a) Group I; (b) Group II.

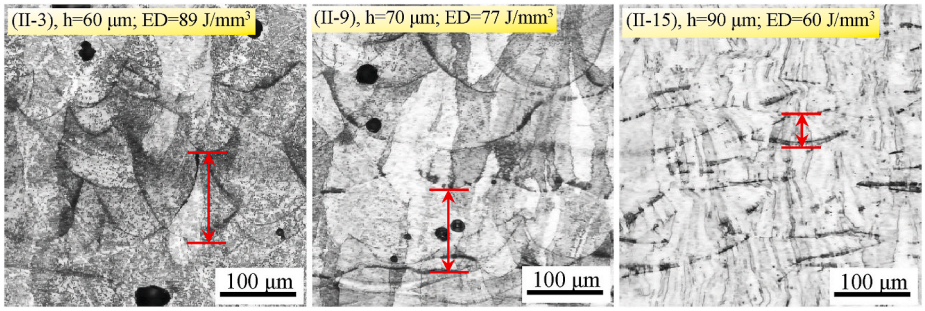

Fig. 4. OM Microstructure of NiTi alloys along the growth direction.

conduction mode. It is obvious that the width and depth of the molten pool increase with the increase of laser energy density. In this experiment, the sample of Group II was selected for analysis. The distance between the lowest points of the boundary lines of two adjacent molten pools, decreases gradually from 112 μm to 61 μm as the hatch spacing value gradually increases from 60 μm to 90 μm, as similar results mentioned in previous research [26].

The transverse corrosion microstructures of two groups of samples are shown inFigure S5 and Figure S6, respectively. It is evident that the transverse microstructure is closely arranged in the shape of small squares when the hatch spacing is 80 and 90 μm. However, when the hatch spacing is reduced to 70 and 60 μm, the transverse microstructure of the samples becomes more complex and chaotic. There is a significant presence of chaotic impurities distributed within the small grid,

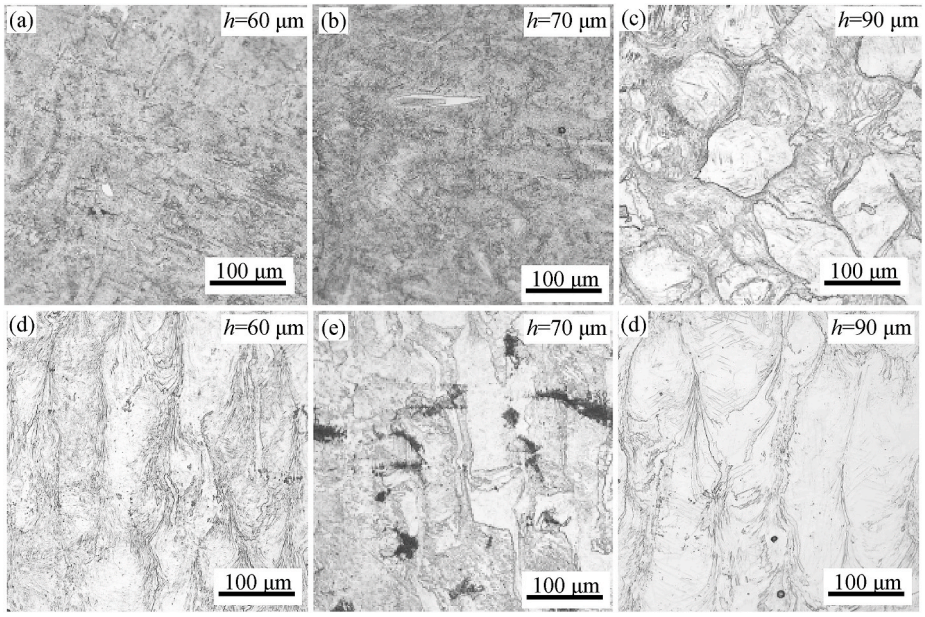

Fig. 5. Effect of hatch spacing on the microstructure of NiTi alloys: (a) (b) transverse direction, (c) (d) along the growth direction; (a) and (d)-No. II-3, (b) and (e)-No. II-9; (c) and (f)-No. II-15.

resulting in an unclear and unclean transverse corrosion structure. Although the small grid morphology is still discernible, as shown in Fig. S6. The typical transverse microstructure of samples prepared using different hatch spacing is shown in Fig. 5(a) and Fig. 5(b).

The longitudinal corrosion microstructures of the two groups of samples are depicted in Figure S7 and Figure S8,respectively. It is evident that columnar crystals are present in all samples along the building direction. This implies that despite a 67° rotation angle difference between adjacent layers during printing, the formation of columnar crystals cannot be eliminated. Moreover, when the laser energy density is high (samples located in the lower left corner area of the diagonal in Fig. S7), the columnar crystals exhibit a river-like morphology with disordered growth directions. The river-like morphology of the dendrites becomes more pronounced as the energy density increases, leading to a higher density of dendrite boundaries and a more chaotic direction of growth. Conversely, when the energy density is lower (samples in the upper right corner area of the diagonal in Fig. S7), columnar crystals grow parallel to the building direction, resulting in a lower density of dendrite boundaries. This makes the interior of the dendrites appear cleaner, as depicted in Fig. S7. The effect of energy density on dendrite morphology follows a similar pattern in Fig. S8. The typical columnar crystal structures of samples prepared using different hatch spacing are shown in Fig. 5 (c) and 5 (d).

3.4. Phase transformation behavior

The DSC test results of the selected samples are presented in Fig. 6. Based on Fig. 6(a), it is obviously that the transformation temperature increases with increasing energy density when there is only one independent variable. However, it should be noted that the transformation temperature and energy density no longer follow a simple and strict linear relationship when the independent variables are multiple factors, as shown in Fig. 6(b). This phenomenon also be founded by some researchers [20]. The transformation temperature decreases as hatch spacing increases when the independent variable is only *h*, as shown in Fig. 7. Part of detailed transformation temperature data can be found in Table 4.

The change in elemental composition in NiTi alloys is the primary reason for the effect of energy density on the phase transformation temperature. When the energy density is higher, the Vapor pressure of Ni element decreases compared to Ti, resulting in easier evaporation of Ni. Consequently, the content of Ni element in the matrix is relatively reduced, leading to an increase in the phase transformation temperature [27].

3.5. XRD

The XRD test results for the NiTi alloys samples fabricated by LPBF are depicted in Fig. 8. The figure reveals the presence of B2 austenite as well as a minor amount of B19' Martensite in the block samples.

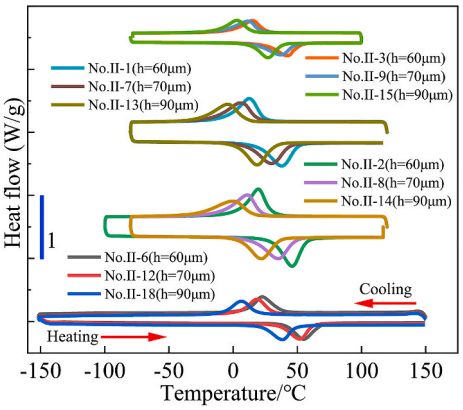

Fig. 7. The DSC curves of LPBF-fabricated NiTi alloys samples, group II.

3.6. Grain characteristics

No. I-13, No. I-14, No. I-20, No. I-21, No. I-27 and No. I-28 samples with energy densities of 69, 83, 63, 73, 58 and 67 J/mm^3 were chosen to investigate the impact of energy density on grain size. Similarly, samples with hatch spacing of 60, 70, 80, and 90 μm were selected to examine the effect of hatch spacing on grain size. These selected samples are indicated by red dashed boxes inFigure S2 and Figure S3. The grain structure of the samples was analyzed using EBSD testing, and the results are displayed in Fig. 9 and Fig. S9.

To prevent the formation of thick and continuous elongated columnar crystals along the building direction in the samples, a layer-by-layer rotation strategy of 67° was implemented in the printing scheme. However, it is evident that columnar crystals did appear along the building direction in all samples. Nonetheless, it is important to note that these columnar crystals display a discontinuous, Z-shaped structure. This indicates that the printing strategy of rotating 67° layer by layer effectively interrupts the growth of columnar crystals and refines the grains.

Furthermore, numerous small equiaxed crystals emerged in the samples, primarily distributed at the interface between layers. This is mainly attributed to the lower temperature and higher cooling rate at the interface, which hinders the timely growth of grains. Additionally, the orientation distribution of grains is random.

The IPF graph results obtained from EBSD testing are presented in Fig. 10 and Fig. S10, revealing contrasting silk texture distributions in samples No. I-13, No. I-14, No. I-20, No. I-21, No. I-27 and No. I-28. It is obvious that when the scanning rate is ≤ 800 mm/s, the texture along the [001] direction is very obvious in samples No. I-13, No. I-14, No. I-20 and No. I-21. However, when the laser power is increased to 1000 mm/s,

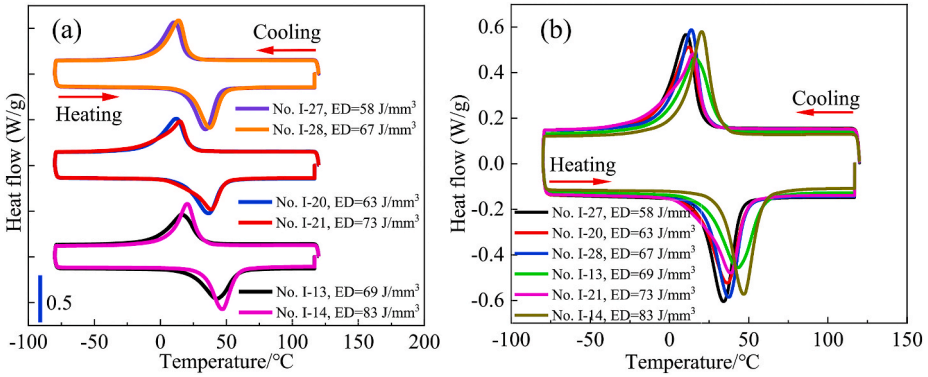

Fig. 6. DSC curves of group I NiTi alloys samples: (a) Compare in groups; (b) compare within the same group.

Table 4
The transformation temperatures and enthalpy changes of NiTi alloys samples fabricated by LPBF.

No.	*ED*	M_s	M_p	M_f	A_s	A_p	A_f	ΔH
No. II-3 (h = 60 μm)	89	30.05	19.66	4.07	30.70	45.99	57.17	23.87
No. II-9 (h = 70 μm)	77	22.24	10.94	−10.03	14.80	35.24	48.57	23.16
No. II-15 (h = 90 μm)	60	15.75	−0.65	−28.11	5.28	22.09	36.56	20.83

Notes: *ED* - Energy density/J/mm^3; M_s - The starting temperature of Martensite transformation, °C; M_p - The peak temperature of Martensite transformation, °C; M_f - The end temperature of Martensite transformation, °C; A_s - The starting temperature of Austenite transformation, °C; M_p - The peak temperature of Austenite transformation, °C; A_f - The end temperature of Austenite transformation, °C; ΔH - Enthalpy, J/g.

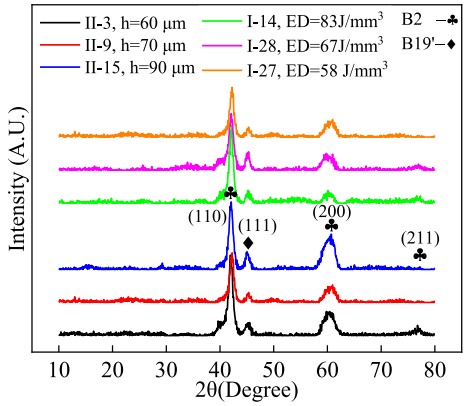

Fig. 8. XRD detection results of NiTi alloys samples prepared by LPBF: the effect of energy density on phase composition in NiTi alloys; the effect of hatch spacing on the phase composition of NiTi alloys.

there is no obvious texture in samples No. I-27 and No. I-28. This pattern can also be observed in Fig. S9. This may be because when the scanning speed is too large, the difference in temperature gradients in various directions inside the sample is not very large, making the growth direction of the texture more random.

In addition, when only the hatch spacing is altered while maintaining the same scanning speed and laser power, evident silk texture along the [001] direction is observed in all samples (No. II-3, No. II-9 and No. II-15). This is primarily due to the higher temperature gradient parallel to the building direction, promoting the directional growth of grains, as previously documented [28]. Furthermore, with the increase of hatch spacing, the strength of the texture along the [001] direction in the sample tends to gradually increase. This is mainly because the change of hatch spacing will change the morphology of the molten pool, thereby changing the direction of the highest temperature gradient, and ultimately changing the direction and strength of the texture [29,30].

3.7. TEM microstructure of NiTi alloys samples

3.7.1. Dislocations

The TEM images in Fig. 11 depict the NiTi alloys samples, revealing the presence of numerous dislocation networks. It is obvious that the dislocation density in the sample gradually increases with the increase of energy density. Especially in the I-14 and II-6 samples with higher energy density, many dislocations are accumulated and tangled together, and dislocation walls are even formed in local areas because the dislocation density is too high.

There is high density of dislocations in NiTi alloys samples prepared by LPBF, these high-density dislocations result from non-equilibrium rapid solidification and significant residual thermal stress during the

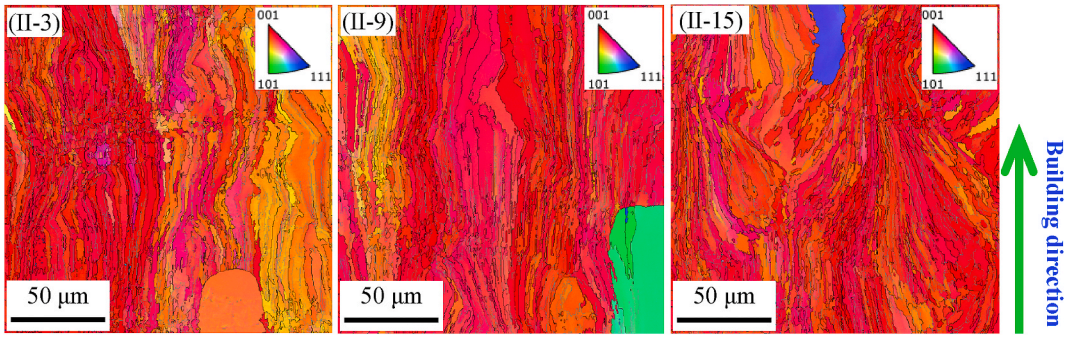

Fig. 9. EBSD morphology of NiTi alloys samples along the building direction.

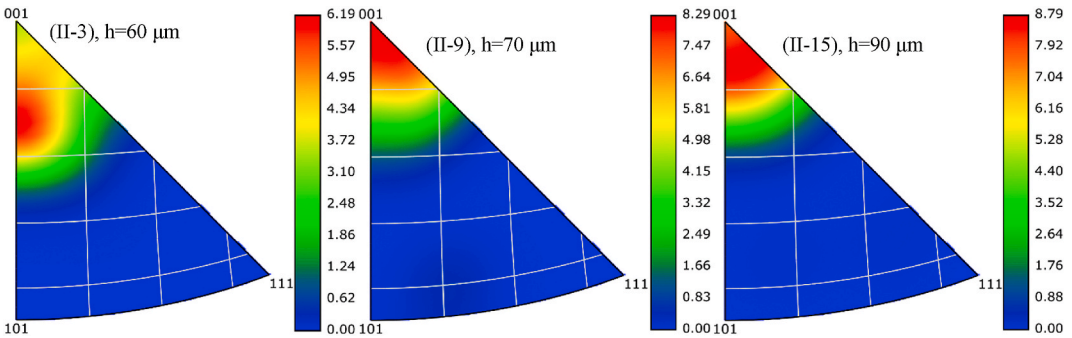

Fig. 10. Reverse polarity diagram of EBSD of NiTi alloys sample.

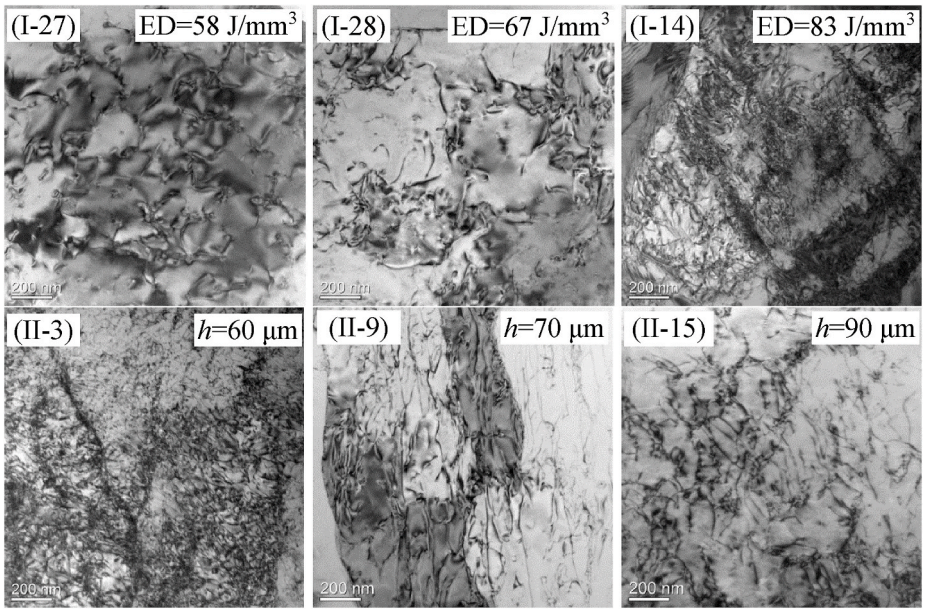

Fig. 11. TEM images of dislocations in NiTi alloys prepared by LPBF.

LPBF process [31]. The cooling rate of the molten metal increases with the increase of laser energy density. At the same time, the non-equilibrium solidification of the molten metal becomes more serious, and the residual stress in the solid sample is higher, which ultimately leads to a higher dislocation density in the sample.

3.7.2. Precipitates

Fig. 12 displays the TEM image of precipitates within the NiTi alloys, revealing the formation of spherical nano-sized precipitates dispersed throughout the matrix. These precipitates may be Ti_4Ni_2O. Additionally, a coherent interface is observed between these nano-sized precipitates and the B2 austenite matrix. This coherent interface induces significant lattice distortion at the interface, resulting in the development of a stress/strain field surrounding the nano-precipitate phase [32].

3.8. Superelasticity and elastocaloric effects of NiTi alloys samples

The hyperelastic stress-strain curves of 6 groups of samples during loading and unloading cycles are shown in Fig. 13 and Fig. S11. During the loading process, there are obvious stress platforms on the curves, corresponding to the characteristics of stress induced martensitic transformation. After 10 cycles, the recoverable strain rates of 6 groups of samples were 60.50%, 75.24%, 67.10%, 79.17%, 66.83%, and 80.17%, respectively. Among them, No. I-28 shows the best recoverable strain.

Fig. 14 and Fig. S12 illustrates the elastocaloric cooling effects of six samples. These results exhibit a consistent trend, wherein the cooling value in the first cycle is the highest, and subsequently decreases gradually as the number of cycles increases. In addition, a comparison of the cooling values for the 1st, 5th, and 10th cycles reveals that the No.1-28 samples exhibit the most favorable cooling effect. Specifically, the

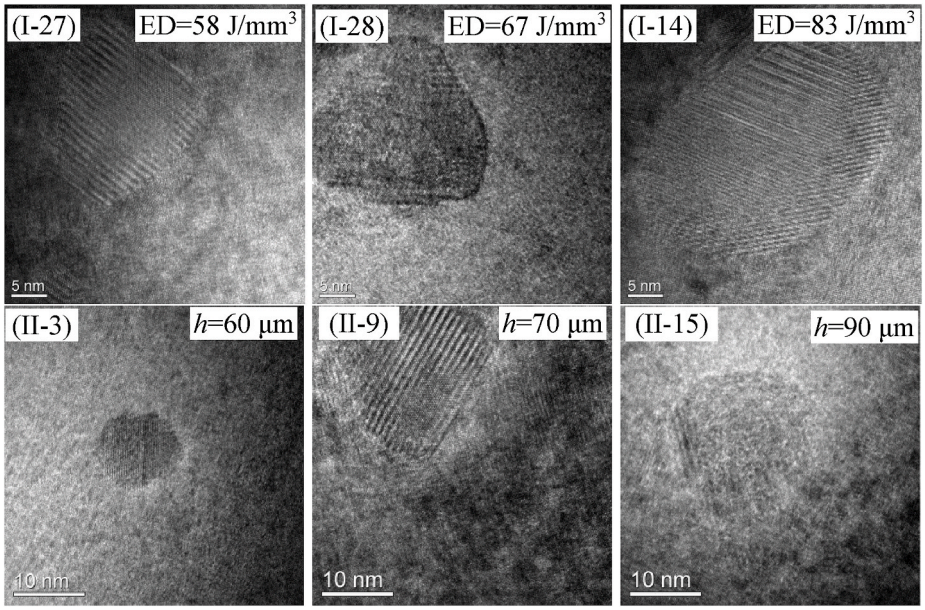

Fig. 12. TEM images of precipitates in NiTi alloys prepared by LPBF.

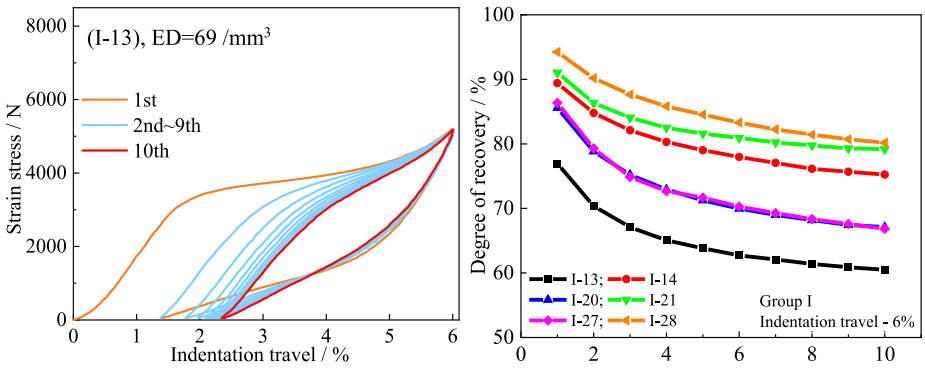

Fig. 13. Superelasticity of the as-built NiTi alloys fabricated by LPBF (with a strain rate of 10^{-4} s^{-1}, at A_f+10 K, the compressive strain is 6%).

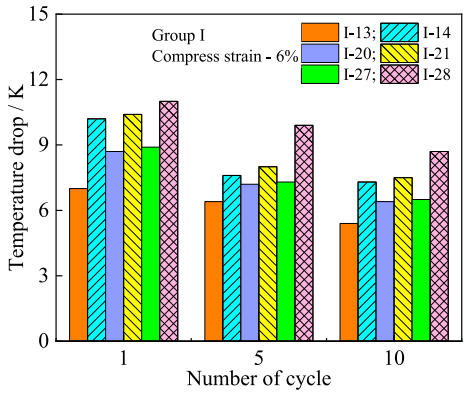

Fig. 14. Temperature variation during the 1st, 5th and 10th cycles of unloading (with a strain rate of 0.6 s^{-1}, at A_f+10 K, 6% compressive strain) and holding, shown as a function of time, for the as-printed NiTi alloys manufactured by LPBF.

cooling temperature differences for the 1st, 5th, and 10th cycles are 11.0 K, 9.9 K, and 8.7 K, respectively.

4. Discussion

4.1. Composition and A_f of NiTi alloys

Changes in laser process parameters have a significant impact on the composition, structure and properties of NiTi alloys. In this experiment, the most important factor is the energy density of the laser, it can be described as **Equation (1)** [32]:

$$ED = \frac{P}{vh} \tag{1}$$

Where ED is Energy density, J/mm^3; P is laser powder, W; v is scanning speed, mm/s; h is hatch spacing, μm.

Under the same conditions, since the vapor pressure of Ni element is lower than that of Ti element, the evaporation amount of Ni element is greater during the sample preparation process. Through calculation and research, Lu found that in the main temperature range of the additive forming process of 1500–3000 K, the volatilization rate of Ni element is 5–10 times higher than that of Ti element [33]. On the other hand, the evaporation amount of Ni element will increase with the increase of laser energy density [34]. Therefore, as the energy density gradually increases, the number and size of porosities in the sample will gradually increase. At the same time, the relative density of the sample will gradually decrease.

The powder undergoes a process of melting and then solidifying during sample preparation. The cooling rate of the droplets during the solidification process increases with the increase of laser energy density, and the residual stress in the structure also follows the same pattern. When the laser energy density is too high, the residual stress in the NiTi alloys sample is too large, which will cause cracks in the sample, as shown in Fig. 2(a). When the energy density of the laser is too low to melt the NiTi alloys powder, un-melted powder will appear in the sample and become a defect in the sample, as shown in Fig. 2(b).

The composition of NiTi alloys has a very sensitive and significant impact on its phase transformation temperature. Many previous studies have shown that every 0.1 wt% increase in the mass fraction of Ni element in NiTi alloys can increase the austenite transformation temperature A_f by approximately 10 K [35]. The evaporation amount of Ni element gradually increases with the increase of laser energy density. Correspondingly, the content of remaining Ni element in the NiTi alloys sample gradually decreases. Therefore, the phase transformation temperature A_f of NiTi alloys samples increases with the increase of laser energy density, as shown in Fig. 6.

4.2. Microstructure of NiTi alloys

4.2.1. The morphology of laser beam boundaries

Normally, the cross-section of laser beam boundaries is a parallelogram, as shown inFigure S5 and Figure S6. But when the value of the hatch spacing is too small, it will be difficult to distinguish the laser beam boundaries. This is primarily due to an increase in the density of laser trajectories, dendrites, and precipitates in the sample as the hatch spacing decreases. These microstructures intertwine and mix after corrosion, ultimately making it difficult to distinguish the square grain boundaries of the grains [12]. This situation also occurs in the longitudinal section of the grain. In detail, the longitudinal section of the grain is generally a long strip along the building direction, and the laser beam boundaries is often relatively clear. But when the hatch spacing is too small, the melt pool boundary will become difficult to discern for the same reason, as shown in Fig. S8.

4.2.2. Grain characteristics

The grains of NiTi alloys samples prepared by additive manufacturing methods are generally columnar crystals along the building direction. Nevertheless, there are still numerous small equiaxed crystals emerged in the samples, primarily distributed at the interface between layers, as shown in Fig. 9 and Fig. S9. This is mainly attributed to the lower temperature and higher cooling rate at the interface, which hinders the timely growth of grains [26]. There is no obvious pattern between the energy density and the grain boundary angle of the sample. This is mainly because the orientation of the grains is random during the process of nucleation and growth [12].

The higher the energy density of the laser, the greater the cooling rate of the molten pool, the more grain nucleation points, and the shorter the grain growth time, which ultimately leads to a greater percentage of small-sized grains.

4.3. Superelasticity of NiTi alloys

4.3.1. Superelasticity properties of a single sample

Superelasticity and elastocaloric effect in NiTi alloys both originate from stress-induced martensitic transformation. The permanent plastic deformation caused by dislocation slip during the stress-induced martensitic transformation prevents NiTi alloys from obtaining perfect superelasticity and almost reversible temperature changes. During the first loading-unloading cycle, dislocations are created in these samples, leading to permanent plastic deformation, and the dislocation strain field stabilizes some of the stress-induced martensitic variants so that such martensitic variants do not transform back to austenite during unloading [36]. Therefore, when continuing the compression operation, the NiTi alloys sample cannot achieve complete recovery, that is, residual strain appears after unloading, as shown in Fig. S11. The dislocations and remnant martensite generated in the first cycle are located at the "correct" places, creating favorable internal stress for subsequent transformation [37,38] and thus resulting in lower critical stress for stress-induced martensitic transformation in subsequent cycles. In addition, the energy dissipation during phase transformation will be decreased because of initially generated dislocations and remnant martensite. On the one hand this results in lower stresses hysteresis during subsequent compression cycles, and on the other hand it prevents further dislocation generation [37,38]. Therefore, fewer and fewer dislocations and smaller residual strain are generated during subsequent compression cycles [39], This is why starting from the seventh cycle the strain becomes almost completely recoverable and the critical stress and stress hysteresis become nearly stable.

4.3.2. Critical stress and stress hysteresis

When comparing the experimental results of different samples, it can be found that the process parameters influence the critical stress for superelasticity. The content of Ni in binary NiTi alloys has an important influence on their crystal structure. Frenzel et al. [40] found that the gradual destabilization of the B19′ phase is accompanied by a small reduction of the angle β, which brings the geometry of the crystal lattice of the B19' phase closer to that of B2 austenite. Taking samples No. I-13 and No. I-14 as examples, since the Ni content in sample No. I-13 is lower than that in sample No. I-14, the critical stress for transformation from austenite to martensite in sample No. I-13 during compression (i.e., the critical stress for superelasticity) is lower than that in sample No. I-14. This difference becomes more obvious as the number of cycles increases, as shown in Fig. S11. Similar patterns were observed when comparing the results of No. I-20 and No. I-21, and No. I-27 and No. I-28.

In addition, the process parameters affect the stress hysteresis of superelasticity by influencing the Ni content in the NiTi alloys. Many researchers [40,41] have found that an increase in Ni content in binary NiTi alloys will reduce the enthalpy change (ΔH) during martensitic phase transformation. Specifically, the friction barrier that hinders the interfacial motion during the martensitic transformation decreases with increasing Ni content. Thus, the stress hysteresis decreases with increasing Ni content. This pattern can be seen when comparing the results of No. I-13 and No. I-14, No. I-20 and No. I-21, and No. I-27 and No. I-28, especially at the 10th cycle, as shown in Fig. S11.

4.3.3. Degree of recovery

During the compression process, the degree of recovery in NiTi alloys is a function of three factors: activation of the correspondent variant pair (CVP) transformation, CVP detwinning, and the critical stress for austenite/martensite slip [42]. The CVP transformation can generate ΔT_{ad} because it involves the transformation of austenite into martensite. However, CVP detwinning does not contribute to ΔT_{ad} since it only involves the detwinning of martensite, with no transformation from austenite to martensite; thus, no elastocaloric effect is expected [43]. Regarding critical stress, it determines whether the NiTi alloy material undergoes phase transformation from austenite to martensite or permanent plastic deformation. If the critical stress for the transformation of austenite to martensite (the critical stress that triggers superelasticity) is greater than the critical stress for austenite/-martensite sliding, permanent plastic deformation will occur in the NiTi alloy matrix, and no strain recovery will be seen in those parts of the material that underwent plastic deformation.

Taking the above three factors into consideration, to obtain a higher degree of recovery and elastocaloric effect, the critical stress for austenite sliding should be higher, while the critical stress for austenite to martensite transformation should be lower. These two factors can be defined using the resolved shear stress factor (RSSF), also known as the Schmid factor. Both the critical stress for phase transformation and the critical stress for austenite/martensite sliding increase as the Schmid factor decreases. The literature clearly indicates that the Schmid factor is highly dependent on the crystallographic texture of NiTi alloys [44]. The martensite Schmid factor (RSSF) values for <001>, <011>, and <111> crystal orientations under compression mode are 0.4, 0.37, and 0.27, respectively [42].

During the compression process, after the superelasticity strain plateau ends, the sample will continue to deform until it reaches the set strain value (stage: slip of martensite) [45]. At this stage, the sample is primarily in the martensite phase. Therefore, the Schmid factor of the martensite phase and martensite slip are the main influencing factors. The degree of recovery of the samples increases with the increase of P when keeping v unchanged (No. I-13 vs. No. I-14, No. I-20 vs. No. I-21, and No. I-27 vs. No. I-28). Also, taking samples No. I-13 and No. I-14 as examples, the IPF diagram (Fig. S10) shows that the proportion of <001> oriented texture in sample No. I-13 is significantly higher than in sample No. I-14. Combined with the martensite Schmid factor, it can be observed that the stronger the <001> oriented texture, the lower the critical stress for martensite sliding, resulting in a higher proportion of plastic deformation. Therefore, the degree of recovery of sample No. I-13 is smaller than that of sample No. I-14 when the number of compression cycles is the same (Fig. S11). This pattern can be seen when comparing the results of No. I-13 and No. I-14, No. I-20 and No. I-21, and No. I-27 and No. I-28, especially at the 10th cycle, as shown in Fig. S11.

4.4. Elastocaloric effects of NiTi alloys

During the compression process, the NiTi alloy will undergo a small amount of plastic deformation, which will gradually accumulate with the increase in the number of training cycles until it stabilizes. Therefore, only part of the stress-induced martensite will transform back into austenite due to the presence of a small amount of permanent plastic deformation. The volume fraction of martensite taking part in the transformation becomes lower as the number of cycles increases and thus the ΔT_{ad} gradually decreases during cycling (Fig. S12).

The degree of transformation strain determines the temperature drops. When the compression strain is the same, the greater the degree of recovery, the higher the volume fraction of austenite/martensite participating in the phase transformation, and the greater the temperature drops. Taking samples No. I-13 and No. I-14 as examples, when the number of compression cycles is the same, since the degree of recovery of sample No. I-13 is lower than that of No. I-14, its corresponding ΔT_{ad} is also smaller. In addition, since the degree of recovery of sample No. I-13 decays faster, the corresponding ΔT_{ad} decays faster as well. This pattern can be seen when comparing the results of No. I-13 and No. I-14, No. I-20 and No. I-21, and No. I-27 and No. I-28, especially at the 10th cycle, as shown in Fig. S12.

Furthermore, the temperature change, ΔT_{ad}, arising from the reversible transformation between crystal phases has a direct correlation to the entropy change, ΔS, as describe **Equation (2)** [46]:

$$\Delta T_{ad} = -\frac{T}{C_p}\Delta S(T) \tag{2}$$

Where *Cp* is the specific heat capacity and *T* is the test temperature. Thereby, the ΔS is a vital parameter, which govern the maximum potential ΔT_{ad} achievable. The *Cp* of binary equiatomic NiTi alloys is 590 J/kg K [47].

The entropy changes of martensitic transformation can be calculated by **Equation (3)** [41] as follows:

$$\Delta S = -\frac{\Delta H}{T_0} \tag{3}$$

The equilibrium temperatures of martensitic transformation can be calculated by **Equation (4)** [41] below.

$$T_0 = -\frac{M_s + A_f}{2} \tag{4}$$

In this experiment, test temperature $T = A_f + 10$. Therefore, ΔT_{ad} can be calculated by **Equation (5)** below.

$$\Delta T_{ad} = -\frac{2\Delta H^*(A_f + 10)}{C_p^*(M_s + A_f)} \tag{5}$$

The enthalpy changes (ΔH) of the forward and reverse martensitic transformations can be determined by measuring the area under the cooling and heating curves of the DSC results, as shown in Fig. 6. Therefore, for binary equiatomic NiTi alloys, the maximum temperature drops ΔT_{ad} that can be achieved during phase transformation can be calculated according to **Equation (5)**, given that the accurate DSC curve is measured.

Previous studies have shown that there is a certain functional relationship between T_0, M_s M_f, A_s and A_f of binary NiTi alloys and Ni atomic content [48]. This fitting relationship can be expressed by **Equation (6)** [48]:

$$T_{PT} = \left(A + (B^*x_{Ni}) + C^*D^{(x_{Ni}-50)}\right)^*K \tag{6}$$

The fitting parameters A-D for the five phase transition temperatures considered are listed in Table 5 [48].

Jafar et al. [41] studied the relationship between Ni content and enthalpy change in binary NiTi alloys, as shown in Fig. 15. The authors of this manuscript performed a linear fit on the data in Fig. 15 and obtained **Equations (7) and (8)**. Therefore, by combining **Equations (5), (6) and (8)**, the maximum temperature drops ΔT_{ad} that can be produced by the NiTi alloys during phase transformation can be roughly estimated by knowing only the Ni content in the sample.

$$|\Delta H|_{A\to M} = 910.33463 - 17.62239x_{Ni} \tag{7}$$

$$|\Delta H|_{M\to A} = 881.45612 - 17.03284x_{Ni} \tag{8}$$

When LPBF is used to prepare NiTi alloy samples, its process parameters (*P*, *v*, *h*) determine the final Ni content of the sample. However, there is no relevant research reporting a direct functional relationship between process parameters and Ni content. Therefore, the ΔTad is temporarily estimated directly by the NiTi alloy powder composition and LPBF process parameters during phase transformation.

4.5. Statistics and comparison of elastocaloric effect in NiTi alloys

To intuitively and accurately present the elastocaloric effect of NiTi alloys prepared by LPBF, it is useful to compare it with the results of NiTi alloys prepared by traditional methods. Collecting and comparing the temperature drop values reported in the current literature helps illustrate these differences. Fig. 16 and Table S1 summarize the results of the currently published literature on the elastocaloric effect of NiTi-based shape memory alloys during unloading (for LPBF and LENS, all data are elastocaloric effect values of NiTi alloys in the as-fabricated state).

It is obvious that the order of the elastocaloric effect of NiTi alloy samples prepared by different methods is conventional method > LPBF > LENS. This is mainly due to the differences in the microstructures of the NiTi alloy samples. It can also be seen from Fig. 16 that the elastocaloric effect of NiTi alloys prepared by LPBF has not been extensively studied (only reported in four articles), so this field deserves more attention and research. In addition, the results in this work are better compared to other results obtained by LPBF and under the similar compress strain level.

Table 5
Fitting parameters for the correlation between characteristic transformation temperatures and alloy composition for use in **Equation (6)**.

T_{PT}	A	B	C	D
T_0	4732.79168	−87.47527	−0.04448	216.86145
M_S	4511.2373	−83.42425	−0.04753	204.86781
M_F	4400.1481	−81.7914	−0.00347	1776.53709
A_S	4574.29319	−84.44405	−0.17939	61.65767
A_F	4954.34606	−91.49629	−0.13819	86.75202

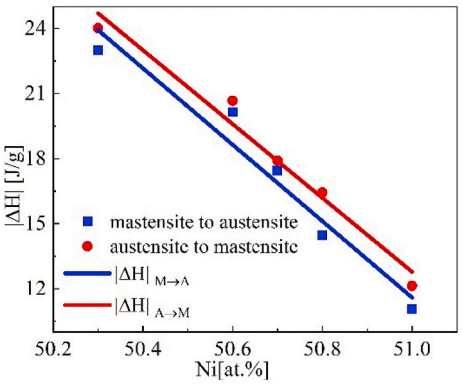

Fig. 15. Enthalpy changes of forward and reverse martensitic transformation as a function of Ni atomic content in binary NiTi shape memory alloys [38].

5. Conclusions

This study focuses on the investigation of the microstructure, phase transformation behavior, and mechanical properties of NiTi alloys manufactured by LPBF. The key findings are as follows:

(1) The optimum energy density range for NiTi alloys is found to be 60–80 J/mm^3, resulting in the highest density, good superelasticity, and elastocaloric effect.
(2) The stress hysteresis decreases with increasing Ni content because the friction barrier that hinders the interfacial motion during the martensitic transformation decreases with increasing Ni content.

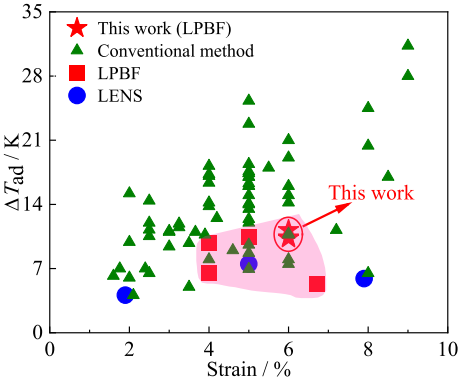

Fig. 16. Comparison of the elastocaloric effects of various shape memory alloys in the literature.

(3) The critical stress for plastic deformation of the texture in the <001> direction in NiTi alloy is the smallest. Therefore, when only the *P* was changed, the proportion of the texture in the <001> direction in the sample increased with the increase of *P*, the proportion of plastic deformation increased, and the degree of recovery also gradually decreased.
(4) When the NiTi alloys undergo the elastocaloric effect, the temperature drop increased with the increase in the degree of recovery when the same compressive strain was selected.

According to the equations established in this study for binary NiTi alloys, a maximum temperature drops when the elastocaloric effect occurs can be approximately predicted based on their composition. However, it worths to further establish a functional relationship between the process parameters during printing and the composition of the NiTi alloy samples, and to eventually constructed a relationship between the composition of the NiTi alloy powder and the temperature drop.

Declaration of competing interest

The authors declare that they have no known competing financial interests or personal relationships that could have appeared to influence the work reported in this paper.

Acknowledgments

This work was supported by a grant from the Department of Industrial and Systems Engineering of The Hong Kong Polytechnic University (project code: G-UAKX), and the Research Institute of Advanced Manufacturing of The Hong Kong Polytechnic University (project code: 1-CD8Y).

Appendix A. Supplementary data

Supplementary data to this article can be found online at https://doi.org/10.1016/j.jmrt.2024.09.081.

References

[1] Miyazaki S. My experience with Ti–Ni-based and Ti-based shape memory alloys. Shape Memory and Superelasticity 2017;3(4):279–314.
[2] Zhu J, Zeng Q, Fu T. An updated review on NiTi alloy for biomedical applications. Corrosion Rev 2019:1–14.
[3] Patel SK, Swain B, Roshan R, et al. A brief review of shape memory effects and fabrication processes of NiTi shape memory alloys. Mater Today Proc 2020;33:5552–6.
[4] Weinert K, Petzoldt V. Machining of NiTi based shape memory alloys. Mater Sci Eng 2004;378(1–2):180–4. SPEC. ISS.
[5] Hassan MR, Mehrpouya M, Dawood S. Review of the machining difficulties of nickel- titanium based shape memory alloys. Appl Mech Mater 2014;564:533–7.
[6] Oliveira JP, Miranda RM, Braz Fernandes FM. Welding and joining of NiTi shape memory alloys: a review. Prog Mater Sci 2017;88:412–66.
[7] Elahinia M, Shayesteh Moghaddam N, Taheri Andani M, et al. Fabrication of NiTi through additive manufacturing: a review. Prog Mater Sci 2016;83:630–63.
[8] Wang X, Kustov S, VAN Humbeeck J. A short review on the microstructure, transformation behavior and functional properties of NiTi shape memory alloys fabricated by selective laser melting. J Mater 2018;11(9).
[9] Oliveira JP, Cavaleiro AJ, Schell N, et al. Effects of laser processing on the transformation characteristics of NiTi: a contribute to additive manufacturing. Scripta Mater 2018;152:122–6.
[10] Guan K. Fundamental study of NiTi shape memory alloy fabricated by selective laser melting[D]. Wuhan: Huazhong University of Science & Technology; 2017.
[11] Xue L, Atli KC, Picak S, et al. Controlling martensitic transformation characteristics in defect-free NiTi shape memory alloys fabricated using laser powder bed fusion and a process optimization framework. Acta Mater 2021:117017.
[12] Saedi S, Shayesteh Moghaddam N, Amerinatanzi A, et al. On the effects of selective laser melting process parameters on microstructure and thermomechanical response of Ni-rich NiTi. Acta Mater 2018;144:552–60.
[13] Speirs M, Wang X, Van Baelen S, et al. On the transformation behavior of NiTi shape-memory alloy produced by LPBF. Shape Memory and Superelasticity 2016;2(4):310–6.
[14] Wang X, Speirs M, Kustov S, et al. Selective laser melting produced layer-structured NiTi shape memory alloys with high damping properties and Elinvar effect. Scripta Mater 2018;146:246–50.
[15] Li S, Hassanin H, Attallah MM, et al. The development of TiNi-based negative Poisson's ratio structure using selective laser melting. Acta Mater 2016;105:75–83.
[16] Franco BE, Ma J, Loveall B, et al. A sensory material approach for reducing variability in additively manufactured metal parts. Sci Rep 2017;7(1):3604.
[17] Saedi S, Turabi AS, Taheri Andani M, et al. The influence of heat treatment on the thermomechanical response of Ni-rich NiTi alloys manufactured by selective laser melting. J Alloys Compd 2016;677:204–10.
[18] Zhang QQ. Study on the microstructural evolution, phase transformation characteristics and property regulation of laser powder bed melted. NiTi shape memory alloys[D]. Jilin, China: Jilin University; 2022.
[19] Wang S. Microstructure and martensitic transformation behavior of NiTi alloy manufactured by selective laser melting[D]. Harbin, China: Harbin Engineering University; 2021.
[20] Das M, Balla VK, Basu D, et al. Laser processing of SiC-particle-reinforced coating on titanium. Scripta Mater 2010;63(4):438–41.
[21] Cao Y, Zhou X, Cong D, et al. Large tunable elastocaloric effect in additively manufactured Ni-Ti shape memory alloys. Acta Mater 2020;194:178–89.
[22] Kordizadeh F, Mohajerani S, Safaei K, et al. Investigating the elastocaloric effect of the NiTi fabricated by laser powder bed fusion: effect of the building orientation. Materialia 2023;30:101817.
[23] Kordizadeh F, Safaei K, Mohajerani S, et al. Investigation of the elastocaloric effect in laser powder bed fusion NiTi porous structures. Additive Manufacturing Letters 2023;6:100131.
[24] Peng X, Ma C, Yuan L, et al. Understanding the role of laser processing parameters and position-dependent heterogeneous elastocaloric effect in laser powder bed fused NiTi thin-walled structures. Smart Mater Struct 2024;33(4):045003.
[25] Parry L, Ashcroft IA, Wildman RD. Understanding the effect of laser scan strategy on residual stress in selective laser melting through thermo-mechanical simulation. Addit Manuf 2016;12:1–15.
[26] Lu HZ. Tailoring mechanisms of functional properties in NiTi shape memory alloys fabricated by selective laser melting[D]. Guangzhou, China: South China University of Technology; 2022.
[27] Sam J, Franco B, Ma J, et al. Tensile actuation response of additively manufactured nickel-titanium shape memory alloys. Scripta Mater 2018;146:164–8.
[28] Yang Y, Zhan JB, Sun ZZ, et al. Evolution of functional properties realized by increasing laser scanning speed for the selective laser melting fabricated NiTi alloy. J Alloys Compd 2019;804:220–9.
[29] Dong Z, Liu Y, Wen W, et al. Effect of hatch spacing on melt pool and as-built quality during selective laser melting of stainless steel: modeling and experimental approaches. Materials 2018;12(1):50.
[30] Saghaian SE, Nematollahi M, Toker G, et al. Effect of hatch spacing and laser power on microstructure, texture, and thermomechanical properties of laser powder bed fusion (L-PBF) additively manufactured NiTi. Opt Laser Technol 2022;149:107680.
[31] Debroy T, Wei HL, Zuback J, et al. Additive manufacturing of metallic components – process, structure and properties. Prog Mater Sci 2018;92:112–224.
[32] Kockar B, Karaman I, Kim JI, et al. Thermomechanical cyclic response of an ultrafine-grained NiTi shape memory alloy. Acta Mater 2008;56(14):3630–46.
[33] Lu BW. Formation and toughening mechanism of direct metal deposited NiTi-based alloys with rare earth modified[D]. Harbin: Harbin Engineering University; 2020.
[34] Xue L, Atli KC, Zhang C, et al. Laser powder bed fusion of defect-free NiTi shape memory alloy parts with superior tensile superelasticity. Acta Mater 2022;229:117781.
[35] Tirry W, Schryvers D. Linking a completely three-dimensional nanostrain to a structural transformation eigenstrain. Nat Mater 2009;8(9):752–7.
[36] Haberland C, Meier H, Frenzel J. On the properties of Ni-rich NiTi shape memory parts produced by selective laser melting. In: Proceedings of the ASME 2012 conference on Smart materials, adaptive structures and intelligent Systems; 2012. p. 97–104.
[37] Yang Z, Cong DY, Sun XM, Nie ZH, Wang YD. Enhanced cyclability of elastocaloric effect in boron-microalloyed Ni-Mn-In magnetic shape memory alloys. Acta Mater 2017;127:33–42.
[38] Ma J, Karaman I, Noebe RD. High temperature shape memory alloys. Int Mater Rev 2010;55:257–315.
[39] Grossmann C, Frenzel J, Sampath V, Depka T, Eggeler G. Elementary transformation and deformation processes and the cyclic stability of NiTi and NiTiCu shape memory spring actuators. Metall Mater Trans A 2009;40:2530–44.
[40] Frenzel J, Wieczorek A, Opahle I, et al. On the effect of alloy composition on martensite start temperatures and latent heats in Ni–Ti-based shape memory alloys. Acta Mater 2015;90:213–31.
[41] Khalil-Allafi J, Amin-Ahmadi B. The effect of chemical composition on enthalpy and entropy changes of martensitic transformations in binary NiTi shape memory alloys. J Alloys Compd 2009;487(1–2):363–6.
[42] Nematollahi M, Saghaian SE, Safaei K, et al. Building orientation-structure-property in laser powder bed fusion of NiTi shape memory alloy. J Alloys Compd 2021;873:159791.
[43] Gall K, Sehitoglu H, Anderson R, et al. On the mechanical behavior of single crystal NiTi shape memory alloys and related polycrystalline phenomenon. Mater Sci Eng, A 2001;317(1–2):85–92.
[44] Gall K, Lim TJ, McDowell DL, et al. The role of intergranular constraint on the stress-induced martensitic transformation in textured polycrystalline NiTi. Int J Plast 2000;16(10–11):1189–214.
[45] Sehitoglu H, Karaman I, Anderson R, et al. Compressive response of NiTi single crystals. Acta Mater 2000;48(13):3311–26.

[46] Mañosa L, Jarque-Farnos S, Vives E, et al. Large temperature span and giant refrigerant capacity in elastocaloric Cu-Zn-Al shape memory alloys. Appl Phys Lett 2013;103(21).

[47] Otsuka K, Ren X. Physical metallurgy of Ti–Ni-based shape memory alloys. Prog Mater Sci 2005;50(5):511–678.

[48] Frenzel J, George EP, Dlouhy A, et al. Influence of Ni on martensitic phase transformations in NiTi shape memory alloys. Acta Mater 2010;58(9):3444–58.